NASA/TM–20220010483

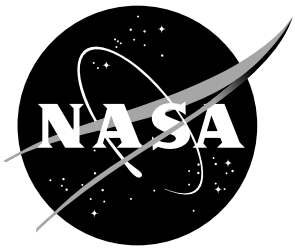

Numerical study of the turbulent Prandtl number in supersonic plane-channel flow – the effect of thermal boundary conditions

D. J. Lusher
Aerodynamics and Flight Mechanics Group, University of Southampton, SO16 7QF UK

G. N. Coleman
Computational AeroSciences, Langley Research Center, Hampton, VA 23681 USA

July 2022

NASA STI Program Report Series

Since its founding, NASA has been dedicated to the advancement of aeronautics and space science. The NASA scientific and technical information (STI) program plays a key part in helping NASA maintain this important role.

The NASA STI program operates under the auspices of the Agency Chief Information Officer. It collects, organizes, provides for archiving, and disseminates NASA's STI. The NASA STI program provides access to the NTRS Registered and its public interface, the NASA Technical Reports Server, thus providing one of the largest collections of aeronautical and space science STI in the world. Results are published in both non-NASA channels and by NASA in the NASA STI Report Series, which includes the following report types:

- TECHNICAL PUBLICATION. Reports of completed research or a major significant phase of research that present the results of NASA Programs and include extensive data or theoretical analysis. Includes compilations of significant scientific and technical data and information deemed to be of continuing reference value. NASA counterpart of peer-reviewed formal professional papers but has less stringent limitations on manuscript length and extent of graphic presentations.

- TECHNICAL MEMORANDUM. Scientific and technical findings that are preliminary or of specialized interest, e.g., quick release reports, working papers, and bibliographies that contain minimal annotation. Does not contain extensive analysis.

- CONTRACTOR REPORT. Scientific and technical findings by NASA-sponsored contractors and grantees.

- CONFERENCE PUBLICATION. Collected papers from scientific and technical conferences, symposia, seminars, or other meetings sponsored or co-sponsored by NASA.

- SPECIAL PUBLICATION. Scientific, technical, or historical information from NASA programs, projects, and missions, often concerned with subjects having substantial public interest.

- TECHNICAL TRANSLATION. English-language translations of foreign scientific and technical material pertinent to NASA's mission.

Specialized services also include organizing and publishing research results, distributing specialized research announcements and feeds, providing information desk and personal search support, and enabling data exchange services.

For more information about the NASA STI program, see the following:

- Access the NASA STI program home page at http://www.sti.nasa.gov

- Help desk contact information:

https://www.sti.nasa.gov/sti-contact-form/
and select the "General" help request type.

NASA/TM–20220010483

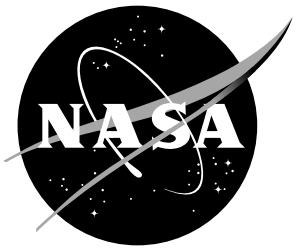

Numerical study of the turbulent Prandtl number in supersonic plane-channel flow – the effect of thermal boundary conditions

D. J. Lusher
Aerodynamics and Flight Mechanics Group, University of Southampton, SO16 7QF UK

G. N. Coleman
Computational AeroSciences, Langley Research Center, Hampton, VA 23681 USA

National Aeronautics and
Space Administration

Langley Research Center
Hampton, Virginia 23681-2199

July 2022

Acknowledgments

We have benefited from discussions with and suggstions by Dr. Robert Baurle, Dr. Dennis Bushnell, Prof. George Huang, Prof. Neil Sandham, and Dr. Philippe Spalart (who suggested the total-flux Prandtl number $\mathrm{Pr}_{\mathrm{tot}}$ as a potentially useful modeling alternative to Pr_t). Thanks are due Dr. Geert Brethouwer and Dr. Hiroyuke Abe for generously providing the passive-scalar DNS data described in Refs. [25] and [26], respectively. D.J.L. gratefully acknowledges support as a visiting researcher at the National Institute of Aerospace, provided by the NASA Langley Research Center (LaRC) under cooperative agreement No. 80LARC17C0004. G.N.C. is supported by the NASA Transformational Tools and Technologies (TTT) Project of the Transformative Aeronautics Concepts Program under the Aeronautics Research Mission Directorate. The open-source OpenSBLI software used in this work was developed under a UK EPSRC Centre for Doctoral Training grant (EP/L015382/1). Computational resources were provided by the NASA LaRC K-cluster and NASA Advanced Supercomputing (NAS) division.

Available from:

NASA STI Program / Mail Stop 148
NASA Langley Research Center
Hampton, VA 23681-2199
Fax: 757-864-6500

Abstract

Direct numerical simulation is used to investigate the turbulent Prandtl number Pr_t above cold (isothermal) and hot (adiabatic) walls in a family of supersonic channel flows. A range of Reynolds numbers and mean temperature/density variations is considered. The value of Pr_t away from the wall approaches 0.85 above both the isothermal and adiabatic walls, with the width of the $\mathrm{Pr}_t = 0.85$ region increasing with wall-variable-based Reynolds number Re_{τ_w} (the latter strongly affected by the thermal boundary condition). The variable, near-wall Pr_t profiles from both the present and previous, passive-scalar simulations collapse as a function of the semilocal y^* wall scaling proposed by Huang et al. [1], with the y^*-dependence weakly parameterized by Re_{τ_w}.

1 Introduction

The objective of this study is to quantify the behavior of the turbulent Prandtl number Pr_t within a subspace of compressible wall-bounded turbulence. Direct numerical simulation (DNS) of supersonic turbulent flow of an ideal gas between two no-slip plane walls – one isothermal, the other adiabatic – is used to isolate the effects of thermal boundary conditions for a range of Reynolds numbers and low-supersonic Mach numbers. DNS of this configuration was first performed by Morinishi, Tamano & Nakabayashi [2] (henceforth MTN03; see also Ref. [3]), who considered a wide range of statistics relevant to turbulence physics and modeling. (The pure/both-wall isothermal case has received relatively more attention; see e.g., Refs. [4–13].) The Pr_t profiles from the wall into the lower core region of the present channel results are expected to be representative of the near-wall and logarithmic regions of zero-pressure-gradient (ZPG) supersonic boundary layers – increasingly so as the Reynolds number increases, both because the body force (i.e., virtual/effective pressure gradient; see below) in wall units approaches zero, and because the logarithmic/inertial sublayer in the 'lower-core' region will become increasingly wide in wall units. For our purposes, an advantage of the channel geometry (in addition to its unambiguous turbulent inflow/outflow boundary conditions) is its relatively small wake component, which allows log-region behavior to persist at much larger fractions of the layer thickness (i.e., channel half-width) than in the boundary-layer counterpart (for which the log layer does not extend beyond 10-20% of the layer thickness [14]).

There have been a number of experimental [15–17] and computational [18–26] studies of Pr_t for low-speed flows. (We limit our attention here to the flow of air; incompressible cases for which the molecular Prandtl number is much larger or smaller than 0.7 are discussed in Refs. [26–28].) These low-Mach number experiments and computations indicate Pr_t approaches a value close to 0.85 in the logarithmic region; cf. [27–29]. A series of recent incompressible/passive-scalar DNS in plane, isoscalar-wall channels has also revealed $\mathrm{Pr}_t \approx 0.85$ within the core region, notwithstanding some slight elements of statistical uncertainty [23–26].

The picture is less precise for high-speed cases, when the scalar becomes active. The question of whether for finite Mach number the log-layer/core Pr_t is variable, approximates 0.85, or some other constant, possibly dependent on thermal boundary conditions, will be addressed below. For reference, the super- and hypersonic boundary-layer DNS of Zhang et al. [30] (the former over an adiabatic wall, the latter over cooled walls) suggest Pr_t is not strongly dependent on freestream Mach number M_∞, or thermal boundary conditions. However, the Reynolds numbers they considered were not large enough to produce pronounced logarithmic layers, and their Pr_t profiles tend to decrease monotonically from a near-wall maximum (near unity) to the edge of the boundary layer (to Pr_t between 0.65 and 0.8 across the five cases); similar behavior was found in the DNS of Liu & Pletcher [31]. On the other hand, the Reynolds number of the Mach 5 boundary-layer experiment of Horstman & Owen [32] was large enough to yield a finite (but thin) log layer, where Pr_t ranged from 0.75 to 0.8. The higher-Reynolds-number, boundary-layer measurements of Sturek & Danberg [33, 34] ($M_\infty = 3.5$, over an adiabatic wall) and Meier [35] ($M_\infty = 5$, over a cold wall) both indicate $\mathrm{Pr}_t \approx 0.8$ as the log-layer value.

The near-wall variation of Pr_t is also of interest. A leading candidate for capturing this variation is the 'semilocal scaling' based on the mean wall-shear stress and local mean density and viscosity: Huang et al. [1] found that in this scaling, the turbulent shear stress and heat flux from (doubly)-isothermal-wall supersonic channel flow at two Mach numbers tend to collapse to a unique profile (see also Refs. [6, 36–38]). The universality of Pr_t as a function of the semilocal wall-normal coordinate y^* (defined below) over a range of mean-property variations within the low-supersonic regime will be a central topic of this paper.

There are undoubtedly many engineering applications for which specifying Pr_t to any order-one value is sufficient. However, there are also cases when a precise value is a great benefit (if only to minimize one element of uncertainty) and others when it is essential. A dramatic example of the latter is provided in Ref. [39], which documents the effect of Pr_t variations when modeling high-speed reacting flows. Those authors demonstrated that setting Pr_t to 0.45, 0.89, and 1.8 resulted in profoundly different predictions of a scramjet combustor, to the extent that some resulted in combustion and some did not. While this example is perhaps extreme, it does illustrate the need to at times prescribe diffusion parameters such as Pr_t as accurately as possible, and thus, serves to highlight the relevance of the present study. The value of this research lies in its aims to reduce physical and statistical uncertainty, and to fill some of the gaps in the parameter space for supersonic wall-bounded turbulence. It is hoped this work will serve as a reliable benchmark and foundation from which studies of other aspects and regimes of compressible turbulence can extend.

2 Problem formulation and cases

The fluid is an ideal gas, with constant-specific-heat ratio $\gamma = 1.4$, and temperature-dependent viscosity $\hat{\mu} = \hat{\mu}_{iw}(\hat{T}/\hat{T}_{iw})^{0.7}$, defined with respect to the (constant) temperature $\hat{T}_{iw}$ and viscosity $\hat{\mu}_{iw}$ at the isothermal wall. (The subscripts iw and aw are used throughout to denote quantities at the isothermal and adiabatic walls, re-

spectively. Dimensional variables are indicated with a caret ($\hat{\cdot}$).) The molecular Prandtl number $\mathrm{Pr} = \hat{\mu}\hat{C}_p/\hat{k} = 0.7$, where $\hat{C}_p$ is specific heat at constant pressure, and $\hat{k}$ thermal conductivity. The plane-channel flow is defined with respect to streamwise $x_1 = x$, wall-normal $x_2 = y$, and spanwise $x_3 = z$ components, in units of the channel half-width $\hat{h}$, with correponding velocity components $u_1 = u$, $u_2 = v$, and $u_3 = w$. To impose a mixed thermal wall configuration, no-slip isothermal and adiabatic walls are located at $y = -1$ and $y = +1$, respectively; these boundary conditions were verified against an analytic laminar solution in Ref. [40]. Periodic boundary conditions are applied in the x and z directions. The domain size is set as $(L_x, L_y, L_z) = (4\pi, 2, 4\pi/3)$, based on Ref. [24], who found for their passive-scalar channel DNS that $\Lambda_x = 2\pi$ and $\Lambda_z = \pi$ are sufficient to produce domain-independent second-order statistics.

In addition to $\hat{T}_{iw}$ and $\hat{h}$, the reference quantities used to nondimensionalize the problem are the bulk-mean density $\hat{\rho}_b = \int_{-\hat{h}}^{+\hat{h}} \langle\hat{\rho}\rangle \mathrm{d}\hat{y}/2\hat{h}$, and the global-mean friction velocity $\hat{v}_\tau$, given by $\hat{\rho}_b \hat{v}_\tau^2 = \left(\langle\hat{\tau}_{iw}\rangle + \langle\hat{\tau}_{aw}\rangle\right)/2$, where $\langle\hat{\tau}_{iw}\rangle$ and $\langle\hat{\tau}_{aw}\rangle$ are the magnitudes of the mean shear stress at their respective walls. (Following Ref. [1], angle brackets $\langle\,\cdot\,\rangle$ are used throughout to denote a Reynolds average, while curly brackets $\{\,\cdot\,\}$ indicate density-weighted/Favre-averaged quantities). The nondimensional governing equations are thus

$$\frac{\partial \rho}{\partial t} + \frac{\partial \rho u_j}{\partial x_j} = 0, \tag{1}$$

$$\frac{\partial \rho u_i}{\partial t} + \frac{\partial}{\partial x_j}\left[\rho u_i u_j + p\delta_{ij} - \tau_{ij}\right] - f\delta_{i1} = 0, \tag{2}$$

$$\frac{\partial \rho E}{\partial t} + \frac{\partial}{\partial x_j}\left[\rho E u_j + u_j p - q_j - u_i \tau_{ij}\right] - f u_1 = 0, \tag{3}$$

where

$$\tau_{ij} = \frac{\mu}{\mathrm{Re}_{v_\tau}}\left(\frac{\partial u_i}{\partial x_j} + \frac{\partial u_j}{\partial x_i} - \frac{2}{3}\delta_{ij}\frac{\partial u_\ell}{\partial x_\ell}\right), \tag{4}$$

$$q_j = \frac{-\mu}{(\gamma-1)M_{v_\tau}^2 \,\mathrm{Pr}\,\mathrm{Re}_{v_\tau}}\frac{\partial T}{\partial x_j}, \text{ and } \mu = T^{0.7}. \tag{5}$$

The total energy E is given by

$$\rho E = \frac{p}{\gamma - 1} + \frac{1}{2}\rho u_i u_i, \text{ with } p = \rho T/\gamma M_{v_\tau}^2. \tag{6}$$

The reference Reynolds number $\mathrm{Re}_{v_\tau} = \hat{\rho}_b \hat{v}_\tau \hat{h}/\hat{\mu}_{iw}$ and reference Mach number $M_{v_\tau} = \hat{v}_\tau/\sqrt{\gamma \hat{R}\hat{T}_{iw}}$ (with $\hat{R}$ the ideal gas constant) are used to define the cases shown in Table 1. Because we consider only 'natural,' internal, turbulence-generated heating, with no external sources or sinks, M_{v_τ} is primarily responsible (along with the thermal boundary conditions) for setting the strength of the mean wall-normal gradients of temperature and density; as we shall see below, M_{v_τ} has only a weak impact on the mean core Mach number. Cases with an 'ai' prefix use the mixed adiabatic/isothermal boundary condition, and 'ii' denotes a doubly isothermal flow.

The streamwise body force f in Eqs. (2) and (3) plays the role of the mean pressure gradient in incompressible channel flows; locally, it will be either proportional to ρ (i.e., $\hat{f} = \hat{\rho}\hat{v}_\tau^2/\hat{h}$) or uniform ($\hat{f} = \hat{\rho}_b\hat{v}_\tau^2/\hat{h}$). Note, the streamwise gradient of the actual, thermodynamic mean pressure $\mathrm{d}\langle p\rangle/\mathrm{d}x = (\mathrm{d}\langle \rho T\rangle/\mathrm{d}x)/\gamma M_{v_\tau}^2$ is zero, as needed for periodic conditions to be appropriate.

Two of the cases, aiD2 and aiF2, (artificially) prescribe Re_{v_τ} with a step function in viscosity at $y = y_0$, with the larger Re_{v_τ} on the adiabatic-wall side, where $y > y_0$ (see Table 1). The value of y_0 is chosen to be where the effect of viscosity on the energy-containing eddies is very weak (the Kolmogorov viscous range of the spectrum will be strongly affected). This is done to optimize the available spatial resolution, to account for the higher viscous effects induced by the higher temperatures on the adiabatic-wall side (see below). For Cases aiD2 and aiF2, the adiabatic-side Re_{v_τ} is set near the largest value the grid will support. The viscosity-jump location, y_0, is an a priori estimate of the effective boundary between the isothermal- and adiabatic-wall layers, which we denote y_e and define as the location at which the wall-normal gradient of the density-weighted/Favre-average velocity, $\mathrm{d}\{u\}/\mathrm{d}y$, is zero (see Fig. 3*c* and Table 4). We choose, for Case aiD2, $y_0 = 0.0872$ (compared to the target, $y_e = 0.141$); for Case aiF2, $y_0 = 0.165$ (compared to $y_e = 0.161$). The Reynolds-number variation for each of the cases, defined in terms of mean profiles, is illustrated in Fig. 6*a*.

3 Numerical approach

All of the cases were simulated with the high-order OpenSBLI flow solver [40]. OpenSBLI has been applied to a wide range of compressible flow problems (Ref. [40] and references therein), including DNS of compressible wall-bounded turbulence [41,42]. Equations (1) – (3) are discretized on an $N_x \times N_y \times N_z$ grid using 4th-order spatial central differences. A 4th-order boundary scheme (Carpenter et al. [43]) is applied near the walls to maintain consistent spatial order throughout the domain. The convective terms of Eqs. (1) – (3) are written in the quadratic-split form of Feiereisen et al. [44], for improved numerical stability via kinetic energy preservation and reduction of aliasing errors. Viscous terms Eqs. (4) and (5) in Eqs. (2) and (3) are solved in Laplacian form by dedicated second-derivative operators to avoid odd-even decoupling phenomena [45]. Time-stepping is performed by a low-storage explicit 4th-order Runge-Kutta scheme [46, 47]. The time step Δt in Table 1 was chosen to satisfy the CFL condition in Ref. [47]; for a few cases, Δt was reduced below the CFL criterion to avoid spurious behavior in the dilatational field at/near the adiabatic wall.

The mesh is uniformly spaced in the homogeneous x and z directions. In the wall-normal direction, a nonuniform stretching is applied as

$$y|_j = \frac{L_y}{2}\left(1 - \left[\frac{\tanh\left(\beta\left(1-2\xi_j\right)\right)}{\tanh\left(\beta\right)}\right]\right) - 1, \tag{7}$$

with stretch factor $\beta = 1.7$ and uniformly distributed points $\xi_j = [0, 1]$ for $j = 0 \ldots N_y - 1$. It was discovered for the present utilization that for the magnitude and

Table 1. Case definitions; spatial and temporal resolution.

Case	Re_{v_τ}	M_{v_τ}	f	$N_x \times N_y \times N_z$	Δx^*	Δy^*	Δz^*	Δx^+	Δy_w^+	Δz^+	$\Delta t \times 10^6$
iiA	190.7	0.0955	ρ	$385 \times 315 \times 211$	4.9^a	0.92^{a}	3.0^{a}	7.3	0.33	4.4	50
aiA	193.9	0.0969	ρ	$385 \times 315 \times 211$	$4.3^b/2.8^c$	$0.88^{\mathrm{b}}/0.75^{\mathrm{c}}$	$2.4^{\mathrm{b}}/1.7^{\mathrm{c}}$	$10.0^d/2.3^e$	$0.45^{\mathrm{d}}/0.10^{\mathrm{e}}$	$6.1^{\mathrm{d}}/1.4^{\mathrm{e}}$	50
aiB	400	0.0955	1	$769 \times 643 \times 427$	$4.7^{\mathrm{b}}/2.6^{\mathrm{c}}$	$0.57^{\mathrm{b}}/0.46^{\mathrm{c}}$	$2.8^{\mathrm{b}}/1.6^{\mathrm{c}}$	$10.5^{\mathrm{d}}/2.3^{\mathrm{e}}$	$0.46^{\mathrm{d}}/0.10^{\mathrm{e}}$	$6.3^{\mathrm{d}}/1.4^{\mathrm{e}}$	25
aiC	600	0.135	1	$845 \times 435 \times 475$	$4.9^{\mathrm{b}}/2.4^{\mathrm{c}}$	$0.90^{\mathrm{b}}/0.68^{\mathrm{c}}$	$2.9^{\mathrm{b}}/1.4^{\mathrm{c}}$	$17.9^{\mathrm{d}}/2.0^{\mathrm{e}}$	$1.27^{\mathrm{d}}/0.14^{\mathrm{e}}$	$10.6^{\mathrm{d}}/1.2^{\mathrm{e}}$	57.5
aiD	780	0.0955	1	$1461 \times 575 \times 799$	$4.8^{\mathrm{b}}/2.5^{\mathrm{c}}$	$0.87^{\mathrm{b}}/0.64^{\mathrm{c}}$	$2.9^{\mathrm{b}}/1.5^{\mathrm{c}}$	$11.2^{\mathrm{d}}/2.1^{\mathrm{e}}$	$1.04^{\mathrm{d}}/0.20^{\mathrm{e}}$	$6.9^{\mathrm{d}}/1.3^{\mathrm{e}}$	45
aiD2	$780^f/1560^g$	0.0955	1	$1461 \times 575 \times 799$	$4.9^{\mathrm{b}}/4.5^{\mathrm{c}}$	$0.88^{\mathrm{b}}/0.84^{\mathrm{c}}$	$3.0^{\mathrm{b}}/2.8^{\mathrm{c}}$	$11.6^{\mathrm{d}}/4.0^{\mathrm{e}}$	$1.02^{\mathrm{d}}/0.37^{\mathrm{e}}$	$7.1^{\mathrm{d}}/2.3^{\mathrm{e}}$	45
aiE	1200	0.20	1	$1021 \times 475 \times 575$	$5.3^{\mathrm{b}}/2.3^{\mathrm{c}}$	$0.93^{\mathrm{b}}/0.66^{\mathrm{c}}$	$3.1^{\mathrm{b}}/1.4^{\mathrm{c}}$	$39.6^{\mathrm{d}}/1.9^{\mathrm{e}}$	$3.10^{\mathrm{d}}/0.15^{\mathrm{e}}$	$23.4^{\mathrm{d}}/1.1^{\mathrm{e}}$	50
aiF2	$1070^{\mathrm{f}}/2354^{\mathrm{g}}$	0.0955	1	$2001 \times 787 \times 1095$	$5.0^{\mathrm{b}}/4.7^{\mathrm{c}}$	$0.77^{\mathrm{b}}/0.75^{\mathrm{c}}$	$3.0^{\mathrm{b}}/2.9^{\mathrm{c}}$	$11.9^{\mathrm{d}}/4.2^{\mathrm{e}}$	$1.10^{\mathrm{d}}/0.38^{\mathrm{e}}$	$7.3^{\mathrm{d}}/2.6^{\mathrm{e}}$	50

[a] At $y^* = 40$.
[b] At $y^*_{iw} = 40$.
[c] At $y^*_{aw} = 40$.
[d] With respect to isothermal/cold wall.
[e] With respect to adiabatic/hot wall.
[f] Isothermal/cold-wall side, $y < y_0$.
[g] Adiabatic/hot-wall side, $y > y_0$.

location of the near/off-wall peak in Pr_t (Fig. 4) to be grid independent, the spatial resolution in terms of the semilocal scaling must not be much larger than $\Delta x^* = 5$, $\Delta y^* = 0.9$, and $\Delta z^* = 3$, at about $y^* = 40$ (i.e., the approximate location of the off-wall peak Pr_t). Given our focus on Pr_t, this criterion was used for all the results presented below.

The $y^* = 40$-based resolution for both sides are summarized in Table 1. Also included are the usual DNS grid measures in wall units, $(\Delta x^+, \Delta y_w^+, \Delta z^+)$, in terms of the density, viscosity and shear stress at each wall (Δy_w is the smallest wall-normal grid spacing, adjacent to the wall). However, the sensitivity to rapid near-wall, mean-property variations makes this measure somewhat arbitrary for cold-wall flows. In CKM95, it was found that DNS using collocation-grid spacings with relatively large values in (cold) wall units can still be fully resolved. For the CKM95 Case B, $\Delta x^+ \approx 39$ and $\Delta z^+ \approx 24$, which are nearly the same as the $\Delta x^+ \approx 40$ and $\Delta z^+ \approx 23.5$ found here for Case aiE (the case for which the difference between the wall-unit and $y^* = 40$ criteria is greatest). The Case aiE wall-normal grid spacing adjacent to the wall is $\Delta y_w^+ \approx 3$, while the tenth grid point (the ninth off the wall) is $y_{10}^+ \approx 29$. Because these are both significantly larger than for Case B ($\Delta y_w^+ \approx 0.2$ and $y_{10}^+ \approx 13.5$), and to account for accuracy differences between the CKM95 fully spectral scheme and the present fourth-order method, Case aiE was repeated using a grid 1.45 times larger in each direction. The results revealed negligible changes to the Pr_t profile near $y^* = 40$, compared to the original results[1]. Since our primary interest is in the behavior of the Pr_t profile, we conclude all the grid sizes shown in Table 1 are sufficient.

The mixed 'ai' cases were initialized with a mature instantaneous field from either the doubly isothermal flow [41] (Case iiA, for Case aiA), or from an 'ai' case at different Re_{v_τ} and M_{v_τ}. For the latter, a cubic-spline interpolation was used to project from a statistically stationary state onto a finer-grid domain once or more. The DNS was then advanced until another stationary state was obtained. The stationary state was identified by monitoring histories of instantaneous wall stress and heat flux at a fixed point on the isothermal wall, and the running-mean values of the density at the centerline and temperature on the adiabatic wall. (For some of the cases, it would have been more efficient to use a Reynolds-averaged Navier-Stokes (RANS) solution to define the initial conditions – especially for Case aiA, since that would have avoided having to capture, via DNS at full resolution, the entire transition from the doubly isothermal flow (iiA) to the mixed/isothermal-adiabatic state; see Fig. 2.)

Statistics were gathered over (x, z) planes and time. The present focus on Pr_t – which, recall, is defined as the ratio of two ratios, each involving a derivative and a second-moment – requires careful consideration of the convergence of the DNS statistics, especially away from the walls, where the 'eddy sample' is smaller. Simulations were continued until the statistics yielded satisfactory balances, both globally and locally in y, of momentum and energy (see Fig. 2*c* and Tables 2 and 3). Fortunately, this produced Pr_t profiles that are reasonably smooth (Figs. 1 and

[1]The value of the off-wall ($y^* \approx 40$) peak Pr_t differed by about 0.3%, while its location varied about 1%.

Table 2. Bulk-mean Reynolds and Mach numbers, and global momentum $\langle \rho u \rangle$ and energy $\langle \rho E \rangle$ balances for cases with density-weighted body force, $f = \rho$. Global-mean wall stress $\langle \tau_w^{\pm} \rangle = \frac{1}{2}\left(|\langle \tau_{12} \rangle|_{y=-1} + |\langle \tau_{12} \rangle|_{y=+1} \right)$. Global-mean heat flux $\langle q_w^{\pm} \rangle = \frac{1}{2}\left(|\langle q_2 \rangle|_{y=-1} + |\langle q_2 \rangle|_{y=+1} \right)$. For Case 2 of MTN03 and Case aiA, $\langle q_w^{\pm} \rangle = \frac{1}{2}\langle q_{iw} \rangle$.

Case	Re_{v_τ}	M_{v_τ}	Re_b	M_b	$\langle T_{aw} \rangle$	$\langle \tau_w^{\pm} \rangle$	$\langle q_w^{\pm} \rangle / U_b$
Ref.[a]	190.7	0.0955	3000	1.5	–	0.996	0.995
iiA	190.7	0.0955	3057	1.53	–	1.003	1.002
Ref.[b]	193.9	0.0969	3000	1.5	2.37	1[c]	0.628
aiA	193.9	0.0969	2910	1.45	3.13	0.999	0.998

[a] Case A of CKM95 [49].
[b] Case 2 of MTN03 [2].
[c] Unity by construction, via definition of body force (MTN03).

4). All the DNS were performed on multi-GPU clusters using CUDA+MPI. For the most expensive case, aiF2, the averaging period was $56.8\hat{h}/\hat{v}_\tau$, over 1.136×10^5 individual fields (one from each 10th DNS timestep). This case required a total of 9,600 GPU hours (16 32GB V100 GPUs $\times$ 600 hours runtime). Minimal-memory storage algorithms [48] were applied to be able to reach a mesh size of $N = 1.7 \times 10^9$ points on a relatively modest number of GPUs.

4 Results

4.1 Validation cases ($f = \rho$)

We begin by applying OpenSBLI to two compressible-channel benchmarks. Both use the density-weighted body force, with $f = \rho$. The first is Case A of Coleman, Kim & Moser [49] (hereafter CKM95), the doubly isothermal supersonic channel flow at bulk Reynolds number $\mathrm{Re}_b = \hat{\rho}_b \hat{U}_b \hat{h}/\hat{\mu}_{iw} = \mathrm{Re}_{v_\tau} U_b = 3000$ and bulk Mach number $M_b = \hat{U}_b / \sqrt{\gamma \hat{R} \hat{T}_{iw}} = M_{v_\tau} U_b = 1.5$, where the bulk velocity $U_b = \int_{-1}^{+1} \langle \rho u \rangle \mathrm{d}y / 2\rho_b$. The good agreement (within 2%) between the bulk Reynolds and Mach numbers for Case iiA and Case A (Table 2) points to the accuracy of this implementation of the OpenSBLI framework. (Recall that for the reference Case A, Re_b and M_b are independent/input parameters, while for Case iiA, Re_{v_τ} and M_{v_τ} are.) Note also the near-unity values of the global momentum and energy balances (which in this nondimensionalization are respectively $\langle \tau_w^{\pm} \rangle$ and $\langle q_w^{\pm} \rangle / U_b$; cf. Eqs. (2) and (3), and see Table 2 legend for definitions). Of even more significance for the present study is the level of correspondence of the Pr_t profiles in Fig. 1.

The second validation run is Case aiA, to be compared to Case 2 of the MTN03 [2] adiabatic-isothermal channel study. The differences (e.g., in the mean adiabatic-wall temperatures $\langle T_{aw} \rangle$; see Table 2) correlate with the degree to which the mean/global energy input by the body force balances the energy flowing out through the lower, isothermal wall, as revealed by the $\langle q_w^{\pm} \rangle / U_b$ ratios. The significant energy imbalance

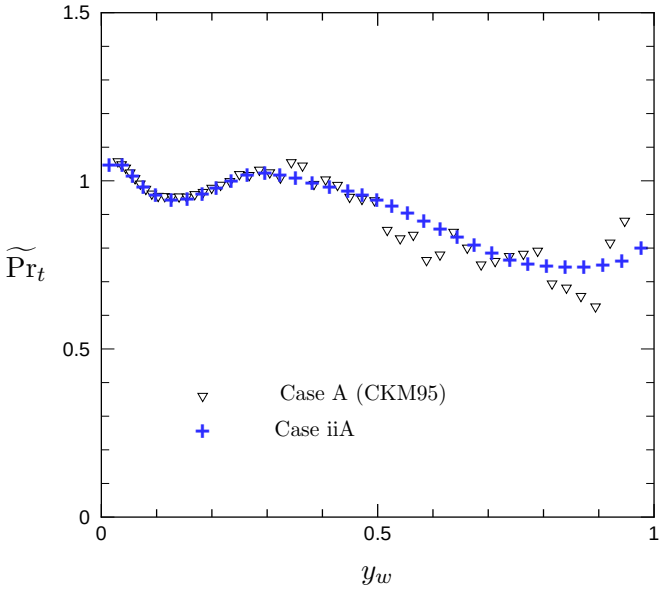

Figure 1. Turbulent Prandtl number, based on Favre-/density-weighted quantities: $\widetilde{\mathrm{Pr}}_t = (\{u''v''\}\mathrm{d}\{T\}/\mathrm{d}y) \,/\, (\{T''v''\}\mathrm{d}\{u\}/\mathrm{d}y)$.

in the MTN03 results reveals the challenge and cost associated with simulating this flow.

The asymmetry introduced by the mixed thermal boundary conditions is evident in all the Case aiA quantities shown, especially the temperature and density fluctuations (Fig. 2*d*). Figure 2*c* presents the terms in the $\langle\rho T\rangle$ balance,

$$\frac{\partial\langle\rho T\rangle}{\partial t} = \frac{\partial}{\partial y}\left[-\langle\rho T v\rangle + \frac{\gamma}{\mathrm{Pr}\,\mathrm{Re}_{v_\tau}}\langle\mu\frac{\partial T}{\partial y}\rangle\right] - (\gamma{-}1)\langle\rho\, T\frac{\partial u_i}{\partial x_i}\rangle + \gamma(\gamma{-}1)M_{v_\tau}^2\,\mathcal{E}, \quad (8)$$

where $\mathcal{E} = \langle\frac{\partial u_i}{\partial x_j}\tau_{ij}\rangle$. The excellent agreement between the flux term and the sum of the pressure-dilatation term and heat-source (from the $\frac{1}{2}\langle\rho u_i u_i\rangle$ dissipation) indicates the quality of the Case iiA and aiA statistics (compare curves and symbols in Fig. 2*c* for each case). Although the pressure-dilatation transfer is significantly larger near the isothermal wall for the mixed-BC flow at nearly the same Re_{v_τ} and M_{v_τ}, and it acts to reduce $\langle\rho T\rangle$ there, both flows are characterized by net generation of heat concentrated near both walls (Fig. 2*c*), leading to nearly uniform $\langle p\rangle = \langle\rho T\rangle/\gamma M_{v_\tau}^2$ and $\sqrt{\langle p'p'\rangle}/\langle p\rangle$ across the channel (Figs. 2*a*, *d*). Because, at equilibrium, the heat generated near both walls exits entirely through the isothermal wall, the mean temperature gradient for Case aiA is everywhere nonzero and positive (Fig. 2*b*). This leads to much higher core temperatures, and thus, much lower mean Mach numbers, at a given M_{v_τ}, compared to the doubly isothermal case. We also note, for future reference, the significantly greater viscous effects associated with higher temperatures on the adiabatic-wall side, for a given Re_{v_τ} (see

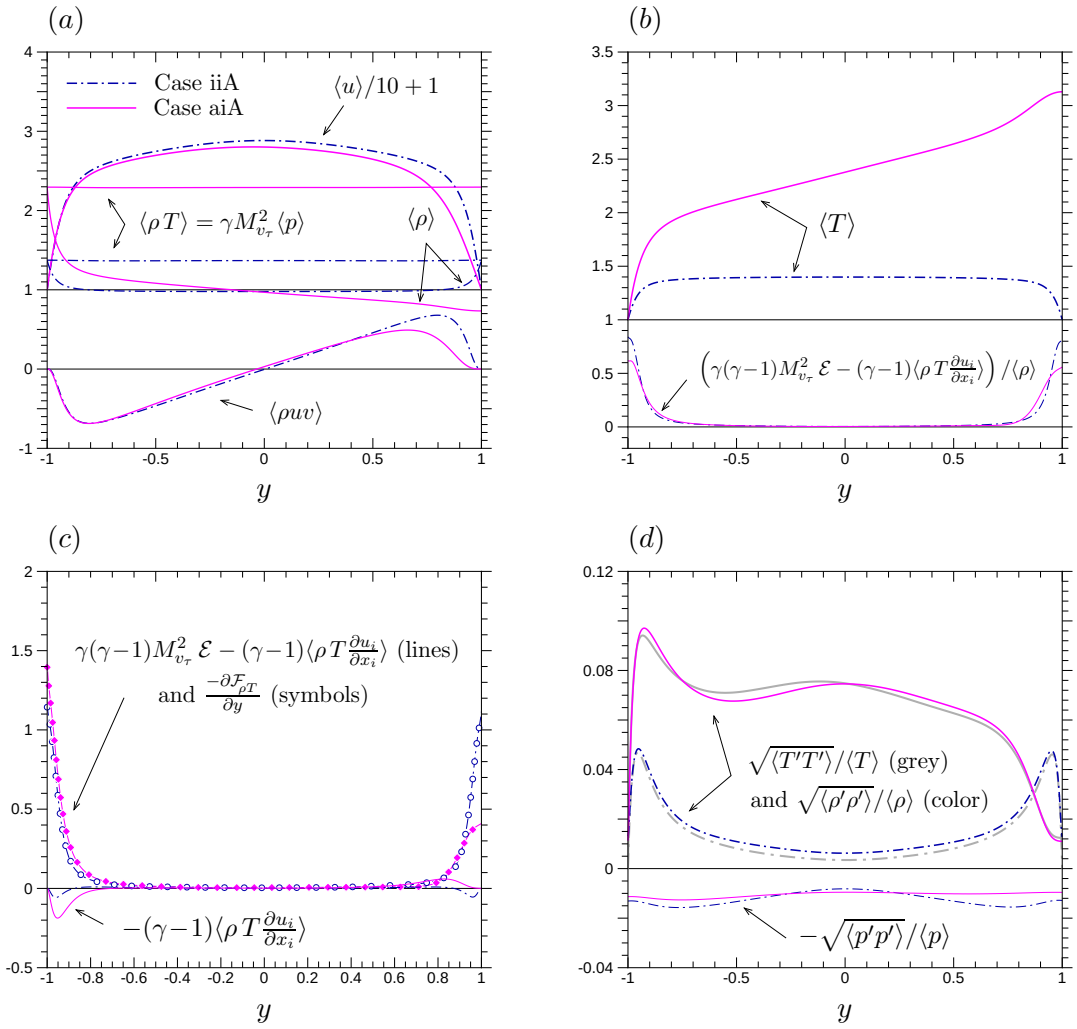

Figure 2. Profiles of (a) mean velocity $\langle u\rangle$, momentum flux $\langle\rho uv\rangle$ and pressure $\langle p\rangle$, (b) mean temperature $\langle T\rangle$ and sum of pressure-dilatation/dissipation terms (per unit mass) in $\partial\langle\rho T\rangle/\partial t$ budget (8), (c) terms in $\langle\rho T\rangle$ budget (8), and (d) temperature, density and pressure fluctuations for density-weighted body-force cases. In (c), flux of $\langle\rho T\rangle$ is $\mathcal{F}_{\rho T}=-\langle\rho Tv\rangle+(\gamma/\mathrm{Pr}\,\mathrm{Re}_{v_\tau})\langle\mu\partial T/\partial y\rangle$.

Table 3. Bulk-mean Reynolds and Mach numbers, and global momentum and energy balances for cases with uniform body force, $f = 1$. Because $f = 1$, the energy balance involves the volume flow rate $Q = \int_{-1}^{+1} \langle u \rangle \mathrm{d}y$, rather than U_b (cf. Table 2).

Case	Re_{v_τ}	M_{v_τ}	Re_b	M_b	$\langle \tau_w^{\pm} \rangle$	$\langle q_{iw} \rangle / Q$
aiB	400	0.0955	6545	1.56	0.996	1.000
aiC	600	0.135	9983	2.25	0.997	0.990
aiD	780	0.0955	13 846	1.70	0.999	0.996
aiD2	$780^a/1560^b$	0.0955	$14\,512^a/29\,024^b$	1.78	0.998	0.994
aiE	1200	0.200	20 638	3.44	0.979	0.955
aiF2	$1070^a/2354^b$	0.0955	$20\,813^a/45\,788^b$	1.86	1.000	1.002

[a] Isothermal/cold-wall side, $y < y_0$.
[b] Adiabatic/hot-wall side, $y > y_0$.

e.g., the $\langle \rho u v \rangle$ profiles in Fig. 2*a*).

4.2 New results ($f = 1$)

Having demonstrated, via Cases iiA and aiA, the accuracy of the OpenSBLI framework, we turn to a series of simulations designed to illustrate the behavior of the turbulent Prandtl number, for various Reynolds and Mach number combinations. To tighten the connection between the present and incompressible channel flows, Cases aiB–aiF2 are driven by a uniform forcing, with $f = 1$ (cf. page 161 of Ref. [49]).

Table 3 presents the bulk- and global-mean results. Both the momentum and energy balances indicate satisfactory levels of equilibrium, in that $\langle \tau_w^{\pm} \rangle$ and $\langle q_{iw} \rangle / Q$ are quite close to one. Since the bulk Mach number M_b is defined with respect to the isothermal wall temperature (and the core temperature is so high), M_b does not correspond to an equivalent freestream Mach number above either of the individual isothermal- or adiabatic-wall layers. Several measures of a more appropriate local/core Mach number are given in Table 4, including the mean (local velocity-magnitude to local sound-speed) Mach number $\langle M \rangle = M_{v_\tau} \langle (u_i u_i)^{1/2} / T^{1/2} \rangle$ at the $\mathrm{d}\{u\}/\mathrm{d}y = 0$ location $y = y_e$, at the channel centerline $y = 0$, and at its maximum, respectively: $\langle M_e \rangle$, $\langle M_c \rangle$, and $\langle M \rangle_{\max}$ (see Fig. 3*a*). A characteristic of this mixed-boundary-condition flow is the weak dependence of the core Mach number on the case-defining reference Mach number (based on the global-mean friction velocity and the isothermal-wall temperature). Note, for example, that the factor of 2.1 increase in M_{v_τ} between Case aiD and aiE, leads to only about a 20% increase in $\langle M_c \rangle$, $\langle M_e \rangle$, and $\langle M \rangle_{\max}$[2]. The highest-speed case (aiE) corresponds to $\langle M_e \rangle = 1.42$, with mean wall-to-edge-temperature ratios of $\langle T_{iw} \rangle / \langle T_e \rangle = 0.12$ and $\langle T_{aw} \rangle / \langle T_e \rangle = 1.5$. Future simulations involving distributed heat sources/sinks will be considered, to allow a broader variation of core Mach numbers.

[2] The turbulence Mach number also shows relatively little variation: $M_t = M_{v_\tau} \langle u_i' u_i' \rangle^{1/2} / \langle T \rangle^{1/2}$ ranges from 0.07 to 0.08 at its minimum, near the centerline, and from 0.20 to 0.25 at its maximum, near the cold wall.

Table 4. Mean core values. Subscripts e and c, respectively, denote quantities at $y = y_e$, the location at which $\mathrm{d}\{y\}/\mathrm{d}y = 0$, and $y = 0$.

Case	y_e	$\langle M_c\rangle$	$\langle M_e\rangle$	$\langle M\rangle_{\max}$	$\langle T_c\rangle$	$\langle T_e\rangle$	$\langle \rho_c\rangle$	$\langle \rho_e\rangle$
iiA	-0.004	1.522	1.522	1.522	1.399	1.399	0.9783	0.9783
aiA	-0.034	1.136	1.136	1.154	2.378	2.360	0.9686	0.9759
aiB	0.074	1.162	1.153	1.167	2.489	2.537	0.9800	0.9615
aiC	0.105	1.327	1.309	1.334	3.955	4.094	0.9728	0.9401
aiD	0.087	1.193	1.182	1.199	2.691	2.758	0.9825	0.9588
aiD2	0.141	1.244	1.228	1.246	2.685	2.797	0.9883	0.9493
aiE	0.116	1.442	1.417	1.455	7.831	8.187	0.9622	0.9206
aiF2	0.161	1.267	1.247	1.268	2.801	2.943	0.9918	0.9447

In terms of the wall-friction Mach number, $M_\tau = \hat{u}_\tau/\sqrt{\gamma\hat{R}\langle\hat{T}_w\rangle}$, where $\hat{u}_\tau = \sqrt{\langle\hat{\tau}_w\rangle/\langle\hat{\rho}_w\rangle}$, at both the isothermal ($M_{\tau_{iw}}$) and adiabatic ($M_{\tau_{aw}}$) walls, the cases span $0.0524 \le M_\tau \le 0.0757$ (Tables 5 and 6). The other inner-layer, compressible-flow scaling parameter, accounting for surface heat transfer, can be written $B_q = (\gamma-1)\langle\hat{q}_w\rangle/\gamma\hat{R}\langle\hat{\rho}_{iw}\rangle\hat{u}_{\tau_{iw}}\langle\hat{T}_{iw}\rangle$ [50]. The variation of this quantity is somewhat wider, with $0.074 \le -B_q \le 0.189$ on the isothermal wall of the $f = 1$ cases (Table 5).

A wall-friction Reynolds number based on the effective-layer thickness,

$$\mathrm{Re}_{\tau_w} = y^+_{e_w} = \langle\hat{\rho}_w\rangle\hat{u}_\tau\hat{y}_{e_w}/\langle\hat{\mu}_w\rangle \tag{9}$$

(where $\hat{y}_{e_w}$ is the wall-normal distance from the wall in question, $\hat{y}_{e_{iw}}$ or $\hat{y}_{e_{aw}}$, to the $\mathrm{d}\{\hat{u}\}/\mathrm{d}\hat{y} = 0$ location $\hat{y}_e$) is displayed in Tables 5 and 6, for both sides of each case. (Note the absence of the channel halfwidth in Eq. (9).) Also included is the Reynolds number, $y^*_{e_{iw}}$ or $y^*_{e_{aw}}$, defined by measuring $\hat{y}_{e_w}$ in the semilocal scaling of Huang et al. [1], for which the nondimensional wall-normal coordinate is given by

$$y^*_w = \langle\hat{\rho}\rangle\hat{u}^*_\tau\hat{y}_w/\langle\hat{\mu}\rangle, \tag{10}$$

where $\hat{u}^*_\tau = \sqrt{\langle\hat{\tau}_w\rangle/\langle\hat{\rho}\rangle}$; thus, $y^*_{e_{iw}} = \sqrt{\langle\hat{\rho}_e\rangle\langle\hat{\tau}_{iw}\rangle}\hat{y}_{e_{iw}}/\langle\hat{\mu}_e\rangle$ and $y^*_{e_{aw}} = \sqrt{\langle\hat{\rho}_e\rangle\langle\hat{\tau}_{aw}\rangle}\hat{y}_{e_{aw}}/\langle\hat{\mu}_e\rangle$. When they are used to sort the cases, the wall-based and semilocal Reynolds numbers give an identical ranking on the hot-wall side, with Cases aiF2 and aiA, respectively, at the high and low extremes. On the cold-wall side (where $\mathrm{Re}_{\tau_{iw}}$ is a much as 12 times larger than $y^*_{e_{iw}}$), the ranking of the cases is identical to that on the hot-wall side, when $y^*_{e_{iw}}$ is used; but when sorted according to $\mathrm{Re}_{\tau_{iw}}$, Case aiE displaces Case aiF2 as having the highest Reynolds number. We shall find that the width of the constant-Pr_t region (as a fraction of the channel halfwidth) correlates better with Re_{τ_w} than it does with $y^*_{e_w}$ (cf. Fig. 6*b*).

Profiles of mean quantities, including those from which the turbulent Prandtl number is built, are shown in Fig. 3. Because the wall-to-wall integral of the rate of kinetic-energy dissipation $\mathcal{E}$ (not shown) is of the same order for all the cases, the mean heat flux through the cold wall and the mean adiabatic wall temperature both increase roughly in proportion to $M^2_{v_\tau}$ (see Eq. (8), and Fig. 3*a*). The subplot in

Table 5. Mean isothermal-wall-side results.

Case	$\mathrm{Re}_{\tau_{iw}} = y^+_{e_{iw}}$	$y^*_{e_{iw}}$	$M_{\tau_{iw}}$	$-B_q$	$\langle T_{iw}\rangle/\langle T_e\rangle$	$\langle \rho_{iw}\rangle$
iiA	224	148	0.0816	0.0499	0.715	1.373
aiA	297	106	0.0671	0.0707	0.424	2.295
aiB	696	228	0.0636	0.0741	0.394	2.431
aiC	1358	251	0.0723	0.1187	0.244	3.826
aiD	1436	426	0.0614	0.0767	0.363	2.634
aiD2	1553	453	0.0630	0.0782	0.358	2.645
aiE	3789	306	0.0757	0.1886	0.122	7.473
aiF2	2234	613	0.0620	0.0799	0.340	2.769

Table 6. Mean adiabatic-wall-side results.

Case	$\mathrm{Re}_{\tau_{aw}} = y^+_{e_{aw}}$	$y^*_{e_{aw}}$	$M_{\tau_{aw}}$	$\langle T_{aw}\rangle$	$\langle T_{aw}\rangle/\langle T_e\rangle$	$\langle \rho_{aw}\rangle$
aiA	73	103	0.0605	3.129	1.33	0.7336
aiB	128	182	0.0588	3.401	1.34	0.7148
aiC	119	184	0.0654	5.873	1.435	0.6515
aiD	227	327	0.0561	3.725	1.35	0.7073
aiD2	401	585	0.0540	3.819	1.365	0.6927
aiE	134	220	0.0689	12.295	1.50	0.6079
aiF2	560	824	0.0524	4.048	1.375	0.6840

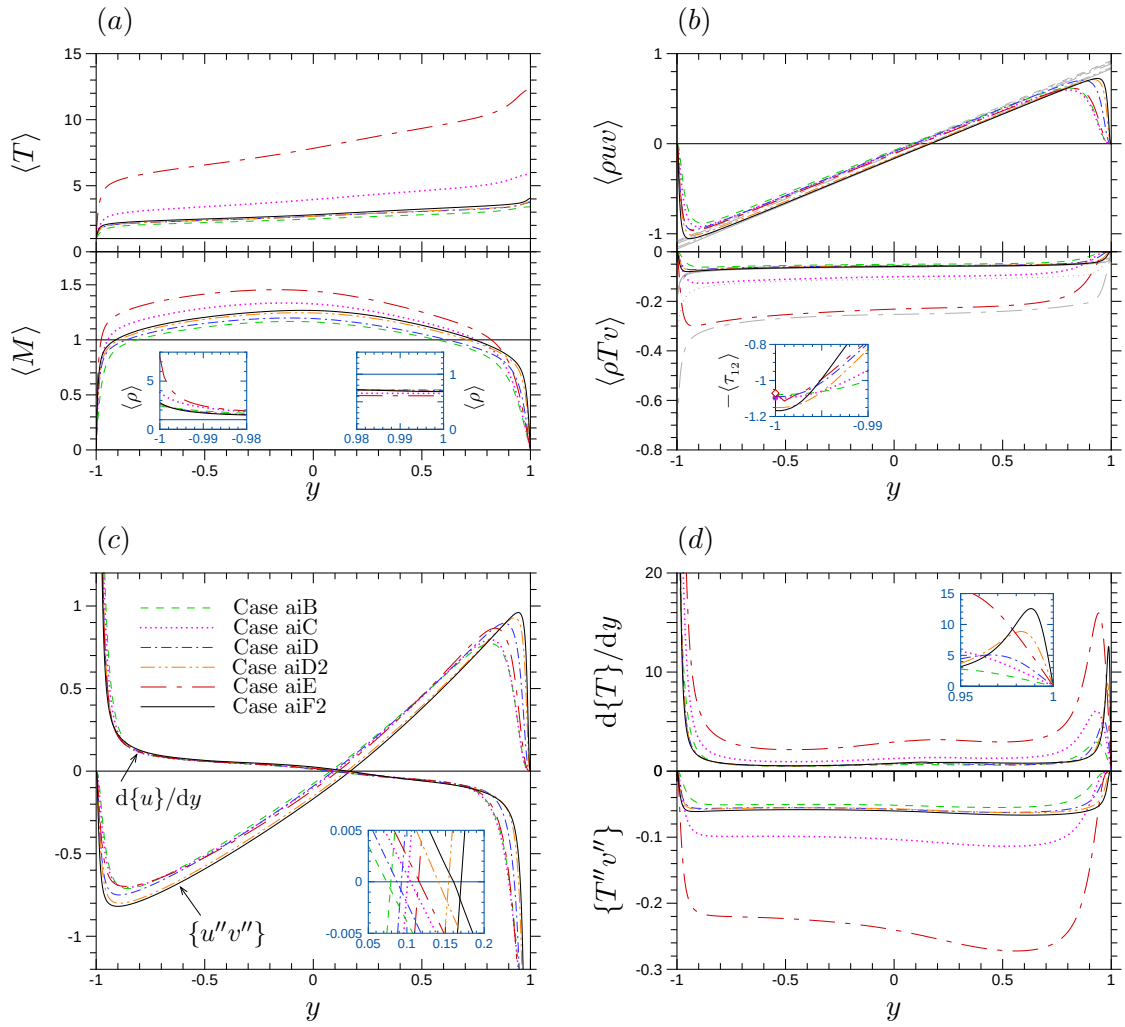

Figure 3. Profiles of (a) mean temperature $\langle T\rangle$, Mach number $\langle M\rangle$ and density $\langle\rho\rangle$, (b) Reynolds-averaged total convective flux of momentum $\langle\rho uv\rangle$ and heat $\langle\rho Tv\rangle$, (c) Favre-averaged velocity gradient $\mathrm{d}\{u\}/\mathrm{d}y$ and turbulent shear stress $\{u''v''\}$, and (d) Favre-averaged temperature gradient $\mathrm{d}\{T\}/\mathrm{d}y$ and turbulent heat flux $\{T''v''\}$, for cases with uniform body force. Mean Mach number $\langle M\rangle = \langle(\hat{u}^2+\hat{v}^2+\hat{w}^2)^{1/2}/\hat{a}\rangle$, with $\hat{a}^2 = \gamma\hat{R}\hat{T}$. Thinner, grey/shaded lines in (b) are (negative) total (viscous plus turbulent) stress or flux, where line type corresponds to case. Symbols in subplot in (b) are wall values for Case aiC (closed circle) and aiE (open diamond).

Fig. 3*c* shows the relationship between the $\{u''v''\} = 0$ and $\mathrm{d}\{u'\}/\mathrm{d}y = 0$ locations. In general, they are quite close, which supports the decision to interpret y_e as the equivalent 'top' or 'edge' location of both the cold- and hot-wall layers. (The outer/core regions of these equivalent layers will of course contain a negligible wake component, so we can only expect the present results to emulate the near-wall and logarithmic regions of spatially developing isothermal- or adiabatic-wall boundary layers.)

For completeness, we note the presence of a weak 'kink' in the y-derivative statistics (mean viscous heat flux and stress) at the first grid point off the isothermal wall in some cases. The severity of this numerical artifact varies in proportion to M_{v_τ}, and is negligible for all but Cases aiC ($M_{v_\tau} = 0.135$) and aiE ($M_{v_\tau} = 0.2$). (See subplot in Fig. 3*b*, and note, in Table 3, the slowly growing deviation from unity with increasing M_{v_τ} of $\langle \tau_w^{\pm} \rangle$ and $\langle q_{iw} \rangle / Q$.) Case aiE was rerun with 1.45-times more grid points in all three directions to check the potential dependence on grid resolution. The artifact remained at the first grid point after refinement, however, suggesting the issue is not related to underresolution[3].

For compressible turbulence, there is some arbitrariness in the definition of Pr_t. We follow Huang et al. [1] and use

$$\widetilde{\mathrm{Pr}}_t = \frac{\widetilde{\nu}_t}{\widetilde{\alpha}_t}, \tag{11}$$

where $\widetilde{\nu}_t = -\{u''v''\}/(\mathrm{d}\{u\}/\mathrm{d}y)$ and $\widetilde{\alpha}_t = -\{T''v''\}/(\mathrm{d}\{T\}/\mathrm{d}y)$. We will also briefly consider the definition used by Zhang et al. [30] when analysing their super- and hypersonic boundary-layer DNS, namely

$$\widehat{\mathrm{Pr}}_t = \frac{\langle \rho u'v' \rangle \mathrm{d}\langle T \rangle/\mathrm{d}y}{\langle \rho T'v' \rangle \mathrm{d}\langle u \rangle/\mathrm{d}y}, \tag{12}$$

to allow direct comparison with their findings. (This quantity is equivalent to the mixing-length factor c introduced by Ref. [1] when examining the performance of the strong Reynolds analogy in purely isothermal-wall channel flow.)

The turbulent Prandtl number profiles in Fig. 4 are the central results of this paper. Please note the Case aiD and Case aiD2 results on the cold-wall side, shown in the subplot in Fig. 4*a*. The very good agreement for $y < -0.5$ supports the dual-viscosity strategy used to maximize the Reynolds number throughout the domain while using a common grid density, for Cases aiD2 and aiF2, since this agreement implies the higher Re_{v_τ} on the hot-wall side has no adverse effect on the lower-Reynolds-number side, well into the core region. The $\widetilde{\mathrm{Pr}}_t$ differences between the aiD and aiD2 results between $y = -0.5$ and 0 reflect 'contamination' from the higher-Re_{v_τ} side, and/or (more likely, in our view) provide a measure of the statistical uncertainty typical of the DNS data, which increases toward the centerline.

The tendency for $\widetilde{\mathrm{Pr}}_t$ to approach a value close to 0.85, at fixed y in the outer/core layer, with increasing Reynolds number – and for the extent of the $\widetilde{\mathrm{Pr}}_t \approx 0.85$ region

[3]The kink also appears in the dilatation field above the isothermal wall for all the cases, except for the doubly isothermal-wall flow, Case iiA. This is presumably due to the global, wall-to-wall nature of the 'acoustic modes' discussed in CKM95, which apparently echo either the symmetry or asymmetry of the thermal boundary conditions.

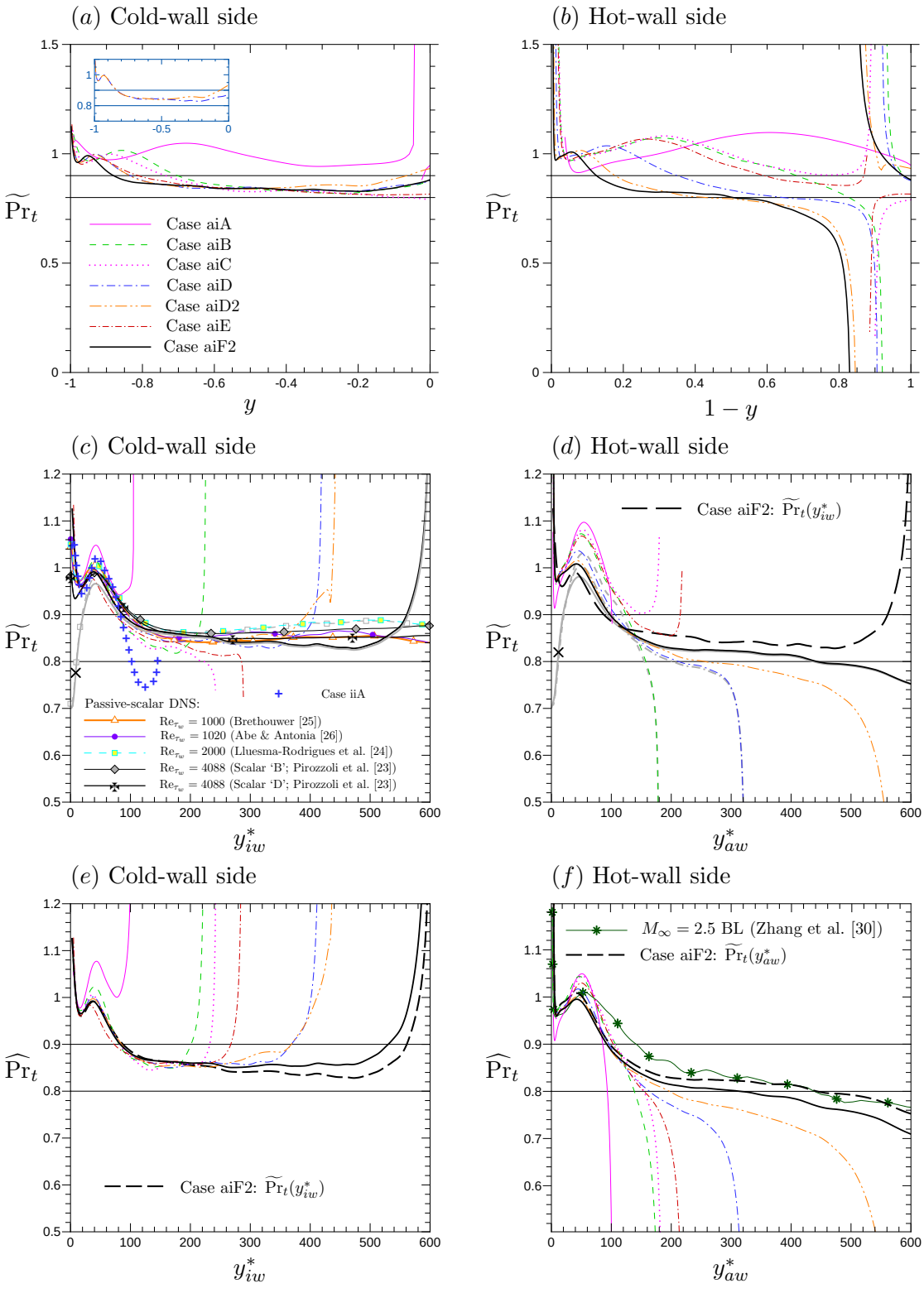

Figure 4. Turbulent Prandtl number. Grey/shaded curves and symbols in (c) and (d) are $\mathrm{Pr}_{\mathrm{tot}}$ profiles for selected cases. Dark cross $\times$ in (c) and (d) denotes location at which $\widetilde{\nu}_t = \langle\hat{\mu}_{iw}\rangle/\langle\hat{\rho}_{iw}\rangle\hat{v}_\tau\hat{h}$ and $\widetilde{\nu}_t = \langle\hat{\mu}_{aw}\rangle/\langle\hat{\rho}_{aw}\rangle\hat{v}_\tau\hat{h}$, respectively, for Case aiF2.

to increase with Reynolds number – is clear, especially on the cold-wall side. Another message from Fig. 4 regards the ability of the semilocal scaling to remove, at least to first order, the significant Reynolds- and Mach-number dependence displayed when the $\widetilde{\mathrm{Pr}}_t$ profiles are presented in units of the channel half-width (Figs. 4*a*, *b*). Figures 4*c*, *d* reveal that for both the cold- and hot-wall layers, the location of the off-wall maximum of $\widetilde{\mathrm{Pr}}_t$ occurs near the same value of y^*_{iw} and y^*_{aw}, of about 40. In contrast, when measured in wall units from the nearest wall, the location of the off-wall peak $\widetilde{\mathrm{Pr}}_t$ moves outward from the cold wall, and toward the hot one, with the width of the $\widetilde{\mathrm{Pr}}_t \approx$ constant regions in Fig. 4 stretching or compressing in proportion to $\mathrm{Re}_{\tau_{iw}}$ or $\mathrm{Re}_{\tau_{aw}}$ (Table 5 or 6). The smaller variations of the off-wall-peak location about $y^*_w = 40$ displayed in Fig. 4*c*, *d* will be examined below. (*Very*-near-wall behavior is not considered here, in order to address only regions of meaningful turbulence transport; the profiles in Fig. 4 do not include near-wall locations for which $-\{\hat{u}''\hat{v}''\}/\hat{v}_\tau^2$ is less than 0.02.)

The colored cross (+) symbols in Fig. 4*c* are from Case iiA. The similarity between the near-wall variation of $\widetilde{\mathrm{Pr}}_t$ in this (purely isothermal) flow and that from the isothermal-wall side of the mixed-boundary-condition cases again underlines the value of the semilocal scaling, and lends further support to the strategy underlying the present study, of interpreting the two sides of the isothermal-adiabatic flow as separate, independent entities, at least with regard to evaluating Pr_t within their near-wall and logarithmic regions. That the Case iiA results, for which $f = \rho$, are in line with the isothermal-wall side results of the $f = 1$ cases (cf. Fig. 5) points to the insensitivity of the $\widetilde{\mathrm{Pr}}_t$ profiles to the body-force weighting, below at least $y^*_{iw} = 80$.

The agreement on the cold-wall side between the present $\widetilde{\mathrm{Pr}}_t(y^*_{iw})$ and the incompressible/passive-scalar results (symbols) is striking, both for the magnitude and location of the off-wall peak, and the $\widetilde{\mathrm{Pr}}_t \to 0.85$ approach at large y^*_{iw}. (Compare the cold- and hot-wall results for $y^*_w > 100$ from Case aiF2 in Fig. 4*d*.) This agreement, which is broadly consistent with the conclusions drawn by Zhang et al. [30] from their DNS of super- and hypersonic boundary layers over adiabatic and cold walls, will be quantified further below.

The relative importance of the molecular and turbulent components of the heat/momentum fluxes can be inferred by considering the ratio of the total (molecular plus turbulent) diffusivities given by

$$\mathrm{Pr}_{\mathrm{tot}} = \frac{\widetilde{\nu}_t + \langle\mu\rangle/\langle\rho\rangle \mathrm{Re}_{v_\tau}}{\widetilde{\alpha}_t + \langle\mu\rangle/\langle\rho\rangle \mathrm{Pr}\,\mathrm{Re}_{v_\tau}}. \tag{13}$$

Comparing $\widetilde{\mathrm{Pr}}_t$ with $\mathrm{Pr}_{\mathrm{tot}}$ (which for selected passive-scalar and compressible cases is shown by the grey/shaded lines/symbols in Fig. 4*c*, *d*) reveals the magnitude of the off-wall peak in $\widetilde{\mathrm{Pr}}_t$ is mitigated (but not eliminated) by inclusion of the molecular terms. (The $\mathrm{Pr}_{\mathrm{tot}}$ ratio may be useful from a practical, modeling point of view, as a replacement for the turbulent Prandtl number, because of this smaller off-wall peak magnitude, and especially its single, well-defined value on the wall, equal to the molecular Prandtl number.) We note the location of the off-wall peak, $y^* \approx 40$, is well above that at which the turbulent and molecular viscosities are equal at both the cold and hot walls: for Case aiF2, these locations are $y^*_{iw} \approx 9$ and $y^*_{aw} \approx 12$

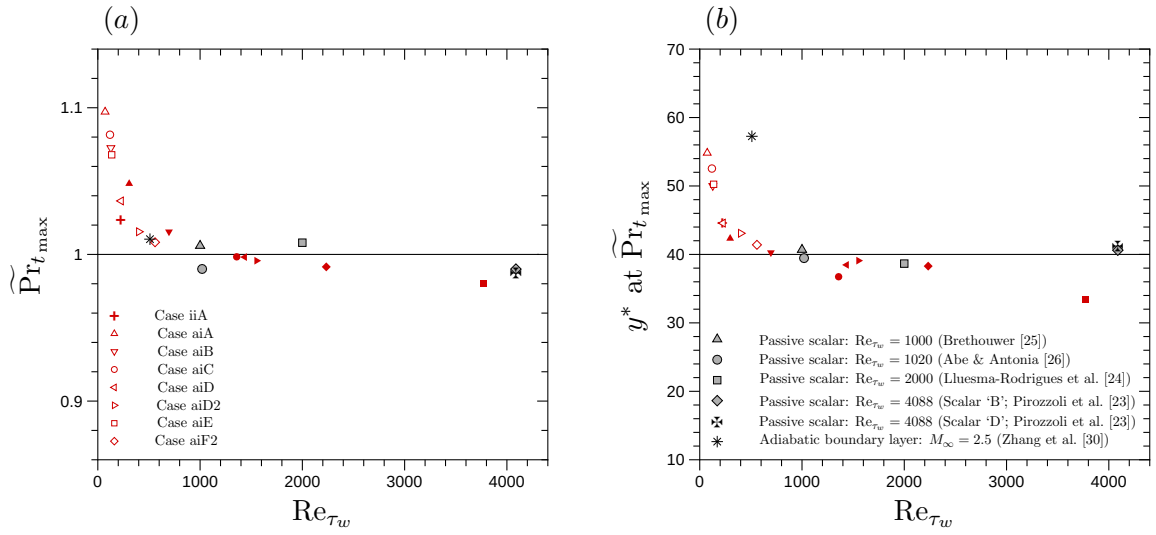

Figure 5. Wall-based Reynolds-number dependence of (a) value and (b) location of off-wall maximum $\widetilde{\mathrm{Pr}}_t$, $\widetilde{\mathrm{Pr}}_{t\,\mathrm{max}}$. Open and closed red symbols are, respectively, from adiabatic-wall and isothermal-wall sides of Cases aiA–aiF2.

(see dark crosses ($\times$) in Figs. 4c, d). The off-wall peak is thus a symptom of the different rates at which the turbulent diffusivities of heat and momentum decrease as they approach the wall: for both sides of all cases, the transport of heat decreases more rapidly with decreasing y_w than the transport of momentum does, until the off-wall peak location, below which the turbulent transport of momentum falls more rapidly [35].

In Figs. 4e, f the alternative definition Eq. (12), for $\widehat{\mathrm{Pr}}_t$, is compared to Eq. (11), for $\widetilde{\mathrm{Pr}}_t$. While the near-wall variation on both sides, below $y^*_{iw} \approx 200$ and $y^*_{aw} \approx 100$, is essentially the same for both expressions (compare thick-long-dash curves and thick-solid curves, for Case aiF2), in the outer/core regions, $\widehat{\mathrm{Pr}}_t$ is more constant than $\widetilde{\mathrm{Pr}}_t$ is on the cold-wall side but less so on the hot-wall side. This difference in the outer region appears to be significant enough to warrant further investigation.

The star symbols in Fig. 4f are from the Zhang et al. [30] adiabatic-wall boundary-layer DNS, with freestream Mach number $M_\infty = 2.5$ and $\mathrm{Re}_{\tau_{aw}} = 510$. The agreement with Case aiF2 ($\mathrm{Re}_{\tau_{aw}} = 560$) is reasonable; the differences exhibited above $y^* = 100$ correlate with differences of the wake components in the channel and boundary layer: for the $M_\infty = 2.5$ boundary layer, the $y_w/\delta = 0.15$ location (a measure of the top of the log layer, where δ is the boundary-layer thickness) corresponds to $y^* = 115$.

The magnitude and location of the off-wall maxima for all the cases, including the incompressible channels and supersonic boundary layers, will be taken up next.

5 Further discussion

In view of the rapid mean-property variations near the adiabatic and especially isothermal walls, and of the success of the semilocal scaling, one might expect the peak value $\widetilde{\mathrm{Pr}}_{t\,\max}$ to be closely correlated with the semilocal Reynolds numbers $y^*_{iw_e}$ or $y^*_{aw_e}$. We find instead the magnitude of $\widetilde{\mathrm{Pr}}_{t\,\max}$ correlates better with the wall-shear Reynolds numbers, $\mathrm{Re}_{\tau_{iw}}$ or $\mathrm{Re}_{\tau_{aw}}$, for both sides (for which, recall, $\mathrm{Re}_{\tau_{iw}} = y^+_{e_{iw}}$ and $\mathrm{Re}_{\tau_{aw}} = y^+_{e_{aw}}$), and all M_{v_τ}, of the present DNS, for incompressible/passive-scalar channels, and for the supersonic ($M_\infty = 2.5$) adiabatic-wall boundary layer [30]; see Fig. 5*a*. The off-wall peak falls with Re_{τ_w} from a maximum near 1.1 to values just below unity; the results for the two highest Re_{τ_w} simulated here (from the cold-wall sides of Cases aiF2 ($\mathrm{Re}_{\tau_{iw}} \approx 2200$) and aiE ($\mathrm{Re}_{\tau_{iw}} \approx 3800$)), and the $\mathrm{Re}_{\tau_w} \approx 4000$ passive-scalar DNS [23], suggests $\widetilde{\mathrm{Pr}}_{t\,\max} \approx 0.98$ may be the high-Re_{τ_w} limit.

The y^* location of $\widetilde{\mathrm{Pr}}_{t\,\max}$ also correlates fairly well with Re_{τ_w}, across the incompressible and compressible channels, and the boundary-layer flow, although there is more scatter for this quantity (Fig. 5*b*). The large deviation of the boundary-layer value is thought to be mostly a consequence of the lack of a well-defined log region for this case, as discussed above, such that the wake component affects the off-wall peak (see Fig. 2a of [30], and recall that $y_w/\delta = 0.15$ corresponds to $z^* = 115$). (That spatial resolution may also contribute to the difference cannot be completely ruled out. Although the Ref. [30] simulation used a 7th-order discretization, and a grid for which, at $y^* = 40$, the streamwise, wall-normal, and spanwise spacings are $\Delta x^* \approx 6.2$, $\Delta y^* \approx 1.3$, and $\Delta z^* \approx 3.7$ (recall the present 4th-order discretization requires $\Delta x^* \leq 5$, $\Delta y^* \leq 0.9$, and $\Delta z^* \leq 3$ at $y^* = 40$ to achieve grid-converged near-wall $\widetilde{\mathrm{Pr}}_t$ profiles), that study employed a WENO-based shock-capturing scheme, which can be less accurate for resolving turbulence than lower-order, nondissipative, central schemes, such as is used here [51]. Pirozzoli [45] recommends 'application [of WENO schemes] to LES and DNS ... only in hybrid form, i.e., in conjunction with a nondissipative algorithm to treat smooth flow zones'. See also [52].) The other outlier in Fig. 5*b* is the $\mathrm{Re}_{\tau_w} \approx 3800$ value from Case aiE. However, the grid-refinement study done for this case, described above, gives some confidence in this result. (The incompressible, passive-scalar DNS all employed nondissipative spatial algorithms and followed standard/well-established resolution guidelines. Nevertheless, it would be interesting to determine whether strict adherence to the $y^*(= y^+) = 40$ criterion required for our code to produce grid-independent near-wall Pr_t profiles (appropriately modified to account for the order of the various schemes[4]) would alter any of the passive-scalar data in Fig. 5.) For now, we interpret Fig. 5 as suggesting the near-wall variation of Pr_t for supersonic wall-bounded turbulence can be usefully approximated as a function of the semilocal coordinate, with that function parameterized by Re_{τ_w} [5].

[4] The resolution used for the fully spectral result from [25] is likely to already satisfy the $y^+ = 40$ criterion.

[5] Compare the proposal by Reynolds [53], that for incompressible/passive-scalar flow at a given molecular Prandtl number, the near-wall Pr_t variation be represented as a unique function of ν_t^+ (the eddy-viscosity profile in wall units) and either y_w^+ or $y_w^+/\mathrm{Re}_{\tau_w}$.

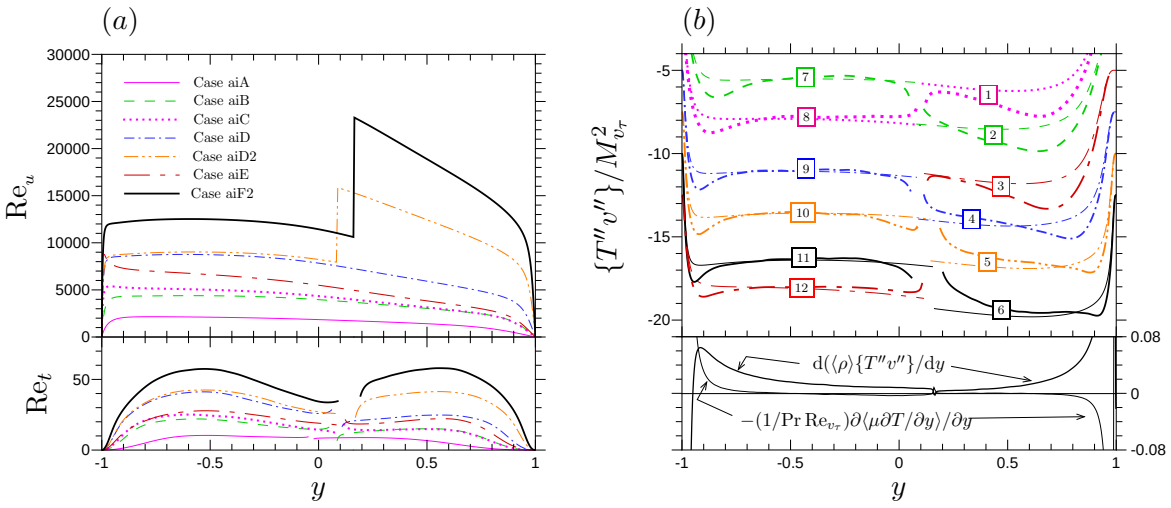

Figure 6. Profiles of (a) local Reynolds numbers, and (b) turbulent heat flux (upper) and viscous and turbulent flux gradients (lower, for Case aiF2 only). Mean-profile Reynolds number $\mathrm{Re}_u = \mathrm{Re}_{v_\tau}\langle\rho\rangle\langle u\rangle/\langle\mu\rangle$; turbulence Reynolds number $\mathrm{Re}_t = \mathrm{Re}_{v_\tau}\langle\rho\rangle\,\widetilde{\nu}_t/\langle\mu\rangle$, where $\widetilde{\nu}_t = -\{u''v''\}/(\mathrm{d}\{u\}/\mathrm{d}y)$. Thicker curves in ($b$) are $-\widetilde{\nu}_t(\mathrm{d}\{T\}/\mathrm{d}y)/0.85$, i.e., the $\widetilde{\mathrm{Pr}}_t = 0.85$ idealization of $\{T''v''\}$ (the latter shown by thinner curves). Heat-flux profiles in (b) each offset vertically by 2.5 units. Number labels on curves correspond to increasing Re_{τ_w} (see Tables 5 and 6).

We conclude by revisiting the large-Re_{v_τ}, $\widetilde{\mathrm{Pr}}_t \to 0.85$ behavior observed in the outer/core regions of Fig. 4. The approach toward the $\widetilde{\mathrm{Pr}}_t = 0.85$ state is revealed in Fig. 6b by the convergence of the (negative) turbulent heat flux $\{T''v''\}$ and $-\widetilde{\nu}_t(\mathrm{d}\{T\}/\mathrm{d}y)/0.85$ with increasing Re_{τ_w}. These two quantities are equivalent when $\widetilde{\mathrm{Pr}}_t$ is exactly 0.85. Also shown in Fig. 6b, in the lower plot, are the molecular and turbulent flux-divergence terms in the $\langle\rho T\rangle$ budget for Case aiF2.[6] (The small 'spikes' at $y = 0.165$ – i.e., at y_0 for Case aiF2 – are due to the step-function change in Re_{v_τ} at this location.) The sum of the two flux-divergence terms in Fig. 6b agrees very well with the sum of the velocity–pressure-gradient correlation, $\frac{\gamma-1}{\gamma}\langle u_i\partial\rho T/\partial x_i\rangle$, and the heat source, $(\gamma-1)M_{v_\tau}^2\mathcal{E}$ (not shown here). For this case, the heat transport due to the turbulence is larger than the molecular transport between $y = -0.925$ and $+0.99$, well into the nearer-wall regions where the $\widetilde{\mathrm{Pr}}_t = 0.85$ relation breaks down. These limits are comparable, but not equivalent, to the near-wall locations at which the turbulent and molecular viscosities are equal, $y = -0.99$ and $+0.98$ (cf. dark cross symbols in Fig. 4c, d).

While the general $\widetilde{\mathrm{Pr}}_t \to 0.85$ trend with increasing Reynolds number is apparent, the $\widetilde{\mathrm{Pr}}_t = 0.85$ condition is more approximate on the hot-wall side, even though the local Reynolds number is not necessarily smaller there: when measured

[6]This form of the $\partial\langle\rho T\rangle/\partial t = 0$ balance, for which γ does not multiply the molecular heat flux, requires modification of the pressure-dilatation correlation in Eq. (8). Recall that for the plane-channel geometry, $\langle\rho Tv\rangle = \langle\rho\rangle\{T''v''\}$.

in terms of turbulence quantities, the Reynolds-number profiles for the two dual-viscosity cases, aiD2 and aiF2, are nearly the same across the two sides (see Re_t in Fig. 6*a*). Additionally, when defined with respect to mean quantities, the magnitude of the hot-wall side profile for these two cases is much larger than on the cold-wall side (see Re_u in Fig. 6*a*). Instead, the approach toward the high-Reynolds-number limit is better characterized by the wall-based Reynolds number Re_{τ_w}. The quality of the $\widetilde{\mathrm{Pr}}_t = 0.85$ idealization improves monotonically with increasing Re_{τ_w}, above both the cold and hot walls. (The curves in Fig. 6*b* are numbered according to Re_{τ_w}, increasing from $\mathrm{Re}_{\tau_{aw}} = 73$ (Curve 1, Case aiC) to $\mathrm{Re}_{\tau_{iw}} = 3789$ (Curve 12, Case aiE).) On the hot-wall side of Case aiF2 (Curve 6), for which $\mathrm{Re}_{\tau_{aw}} \approx 560$ (the largest adiabatic-wall value), the agreement between the actual heat flux and the $\widetilde{\mathrm{Pr}}_t = 0.85$ prediction is comparable, but somewhat worse, than on the cold-wall side of Case aiB (Curve 7), for which $\mathrm{Re}_{\tau_{iw}} \approx 700$ (the smallest isothermal-wall value). The emerging picture of the Pr_t variation for the present flow is thus a function given by $0.85\,\mathcal{F}(y_w^*)$, where $\mathcal{F} \to 1$ for $y_w^* > 100$ or so, provided the Reynolds number is sufficiently large. Below $y_w^* \approx 100$, for any Reynolds number large enough to sustain turbulence, $\mathcal{F}$ at a given y_w^* also depends systematically on Re_{τ_w}.

6 Closing remarks

Our objective has been to isolate the effect of thermal boundary conditions on the turbulent Prandtl number Pr_t in supersonic wall-bounded turbulence. To this end, a new family of DNS has been presented for mixed isothermal/adiabatic-wall plane-channel flows. The two sides of the channel were viewed as independent shear layers, based on the observation that Pr_t above one wall is unaffected by conditions on the opposite-wall side[7]. The parameter space included effective/edge Mach numbers ranging from 1.1 to 1.4, mean wall-to-edge temperature ratios from 0.12 to 1.5, and effective-thickness, wall-friction Reynolds numbers from 73 to 3800.

Validation against previous studies highlighted the difficulty in obtaining converged results for this configuration, and, in particular, avoiding underprediction of the mean adiabatic-wall temperature. Statistics were gathered over sufficiently large time samples to produce good global momentum and energy balances, and smooth Pr_t profiles well into the core region of the channel.

Analogous to the Townsend hypothesis that eddies within the inertial subrange are unaffected by the details of surface roughness (provided the roughness elements are below a certain size threshold), we found here that the details of the surface heat transfer – including its absence – do not prevent the same near-constant Pr_t from appearing in the logarithmic/inertial region above both cold/isothermal and hot/adiabatic no-slip walls. Moreover, the near-wall, nonconstant profile below the inertial sublayer (but well above the *very*-near-wall region, where viscosity dominates) depends – regardless of the thermal-conduction properties of the wall – solely on the wall-variable Reynolds number and a unique function of the mean-density/temperature-weighted semilocal wall-normal variable y_w^*. The extent to

[7]Compare Pr_t above the isothermal wall in Case iiA with that in aiA, and in Case aiD with aiD2.

which this behavior will hold at higher, especially hypersonic, Mach numbers – for which compressibility effects extend well beyond mean-property variations (which dominate in the present supersonic regime), and thermodynamic/dilatational fluctuations become increasingly important – is an open question, requiring further study.

First- and second-order statistics from all the DNS results presented here are available on the NASA Turbulence Modeling Resource (TMR) website[8].

References

1. P. G. Huang, G. N. Coleman, and P. Bradshaw, "Compressible turbulent channel flows: DNS A numerical study of turbulent supersonic isothermal-wall channel flow," *Journal of Fluid Mechanics*, vol. 305, pp. 185–218, 1995.

2. Y. Morinishi, S. Tamano, and K. Nakabayashi, "A DNS algorithm using B-spline collocaiton method for compressible turbulent channel flow," *Computers and Fluids*, vol. 32, pp. 751–776, 2003.

3. Y. Morinishi, S. Tamano, and K. Nakabayashi, "Direct numerical simulation of compressible turbulent channel flow between adiabatic and isothermal walls," *Journal of Fluid Mechanics*, vol. 502, pp. 273–308, 2004.

4. R. Lechner, J. Sesterhenn, and R. Friedrich, "Turbulent supersonic channel flow," *Journal of Turbulence*, vol. 2, pp. 159–183, 2001.

5. Q. Li, *Numerical study of Mach number effects in compressible wall-bounded turbulence*. PhD thesis, University of Southampton, UK, 2003.

6. H. Foysi, S. Sarkar, and R. Friedrich, "Compressibility effects and turbulence scalings in supersonic channel flow," *Journal of Fluid Mechanics*, vol. 509, pp. 207–216, 2004.

7. S. Tamano and Y. Morinishi, "Effect of different thermal wall boundary conditions on compressible turbulent channel flow at $M = 1.5$," *Journal of Fluid Mechanics*, vol. 548, pp. 361–373, 2006.

8. T. Gomez, V. Flutet, and P. Sagaut, "Contribution of Reynolds stress distribution to the skin friction in compressible turublent channel flows," *Physical Review E*, vol. 79, p. 035301(R), 2009.

9. D. Modesti and S. Pirozzoli, "Reynolds and Mach number effects in compressible turbulent channel flow," *International Journal of Heat and Fluid Flow*, vol. 59, pp. 33–49, 2016.

10. M. Yu, C.-X. Xu, and S. Pirozzoli, "Genuine compressibility effects in wall-bounded turbulence," *Physical Review Fluids*, vol. 4, p. 123402, 2019.

[8] https://turbmodels.larc.nasa.gov.

11. M. Yu, C.-X. Xu, and S. Pirozzoli, "Compressibility effects on pressure fluctuations in compressible turbulent channel flow," *Physical Review Fluids*, vol. 5, p. 113401, 2020.

12. M. Yu and C.-X. Xu, "Compressibility effects on hypersonic turbulent channel flow with cold walls," *Physics of Fluids*, vol. 33, p. 075106, 2021.

13. Y. Chen and C. Scalo, "Trapped waves in supersonic and hypersonic turbulent channel flow over porous walls," *Journal of Fluid Mechanics*, vol. 920, p. A24, 2021.

14. I. Marusic, J. P. Monty, M. Hultmark, and A. J. Smits, "On the logarithmic region in wall turbulence," *Journal of Fluid Mechanics*, vol. 716, p. R3, 2013.

15. R. L. Simpson, D. G. Whitten, and R. J. Moffat, "An experimental study of the turbulent Prandtl number of air with injection and suction," *International Journal of Heat and Mass Transfer*, vol. 13, pp. 125–143, 1970.

16. F. Shigetomi and N. Seki, "The behaviour of the temperature-velocity fluctuations and the turbulent Prandtl number in the developing thermal turbulent boundary layer on a flat plate," *Bulletin of the JSME*, vol. 17, no. 105, pp. 351–358, 1974.

17. N. Bagheri, C. J. Strataridakis, and B. R. White, "Measurements of turbulent boundary layer Prandtl numbers and space-time temperature correlations," *AIAA Journal*, vol. 30, no. 1, pp. 35–42, 1992.

18. J. Kim and P. Moin, "Transport of passive scalars in a turbulent channel flow," *Turbulent Shear Flows 6*, pp. 85–96, Springer-Verlag, Berlin Heidelberg, 1989.

19. D. M. Bell and J. H. Ferziger, "Turbulent boundary layer DNS with passive scalars," in *Near-Wall Turbulent Flows* (R. M. C. So, C. G. Speziale, and B. E. Launder, eds.), Elsevier Science Publishers, 1993.

20. M. Kozuka, Y. Seki, and H. Kawamura, "DNS of turbulent heat transfer in a channel flow with a high spatial resolution," *International Journal of Heat and Fluid Flow*, vol. 30, pp. 514–524, 2009.

21. X. Wu and P. Moin, "Transitional and turbulent boundary layer with heat transfer," *Physics of Fluids*, vol. 22, p. 085105, 2010.

22. P. Schlatter, R. Örlü, Q. Li, A. V. Johansson, P. H. Alfredsson, and D. S. Henningson, "Progress in simulations of turbulent boundary layers," *Proceedings of Turbulent Shear Flow Phenomena 7*, Ottawa, 2011.

23. S. Pirozzoli, M. Bernardini, and P. Orlandi, "Passive scalars in turbulent channel flow at high Reynolds number," *Journal of Fluid Mechanics*, vol. 788, pp. 614–639, 2016.

24. F. Lluesma-Rodriguez, S. Hoyas, and M. J. Perez-Quiles, "Influence of the computational domain on DNS of turbulent heat transfer up to $Re_\tau = 2000$ for $Pr = 0.71$," *International Journal of Heat and Mass Transfer*, vol. 122, pp. 983–992, 2018.

25. G. Brethouwer, "Passive scalar transport in rotating turbulent channel flow," *Journal of Fluid Mechanics*, vol. 844, pp. 297–322, 2018.

26. H. Abe and R. A. Antonia, "Mean temperature calculations in a turbulent channel flow for air and mercury," *International Journal of Heat and Mass Transfer*, vol. 132, pp. 1152–1165, 2019.

27. W. M. Kays and M. E. Crawford, *Convective heat and mass transfer*. New York, NY: McGraw-Hill, 1993.

28. W. M. Kays, "Turbulent Prandtl number – where are we?," *Transactions of the ASME: Journal of Heat Transfer*, vol. 116, pp. 284–295, May 1994.

29. A. M. Yaglom, "Similarity laws from constant-pressure and pressure-gradient turbulent wall flows," *Annual Review of Fluid Mechanics*, vol. 11, pp. 505–540, 1979.

30. C. Zhang, L. Duan, and M. M. Choudhari, "Direct numerical simulation database for supersonic and hypersonic turbulent boundary layers," *AIAA Journal*, vol. 56, no. 11, pp. 4297–4311, 2018.

31. K. Liu and R. H. Pletcher, "Compressibility and variable density effects in turbulent boundary layers," *Transactions of the ASME: Journal of Heat Transfer*, vol. 129, pp. 441–448, April 2007.

32. C. C. Horstman and F. K. Owen, "Turbulent preperties of a compressible boundary layer," *AIAA Journal*, vol. 10, no. 11, pp. 1418–1424, 1972.

33. W. B. Sturek and J. E. Danberg, "Supersonic turbulent boundary layer in adverse pressure gradient. Part I: The experiment," *AIAA Journal*, vol. 10, no. 4, pp. 475–480, 1972.

34. W. B. Sturek and J. E. Danberg, "Supersonic turbulent boundary layer in adverse pressure gradient. Part II: Data analysis," *AIAA Journal*, vol. 10, no. 5, pp. 630–635, 1972.

35. H. U. Meier, "Investigation of the heat transfer mechanism in supersonic turbulent boundary layers," *Wärme- und Stoffübertragung*, vol. 8, pp. 159–165, 1975.

36. R. K. Lobb, E. M. Winkler, and J. Persh, "Nol hypersonic tunnel No. 4 result 7: Experimental investigation of turbulent boundary layers in hypersonic flow," NAVORD Report 3880 AD0068499, U. S. Naval Ordnance Laboratory, White Oak, Maryland, 1955.

37. J. C. Rotta, "Über den einfluß der machschen zahl und des wärmeübergangs auf das wandgesetz turbulenter strömung," *Z. Flugwiss*, vol. 7, pp. 264–274, 1959.

38. A. Trettel and J. Larsson, "Mean velocity scaling for compressible wall turbulence with heat transfer," *Physics of Fluids*, vol. 28, p. 026102, 2016.

39. R. A. Baurle and D. R. Eklund, "Analysis of dual-mode hydrocarbon scramjet operation at Mach 4-6.5," *Journal of Propulsion and Power*, vol. 18, pp. 990–1002, 2002.

40. D. J. Lusher, S. P. Jammy, and N. D. Sandham, "Opensbli: Automated code-generation for heterogeneous computing architectures applied to compressible fluid dynamics on structured grids," *Computer Physics Communications*, vol. 267, p. 108063, 2021.

41. A. Hamzehloo, D. J. Lusher, S. Laizet, and N. D. Sandham, "On the performance of WENO/TENO schemes to resolve turbulence in DNS/LES of high-speed compressible flows," *International Journal for Numerical Methods in Fluids*, vol. 93, no. 1, pp. 176–196, 2021.

42. A. Hamzehloo, D. J. Lusher, S. Laizet, and N. D. Sandham, "Direct numerical simulation of compressible turbulence in a counter-flow channel configuration," *Physical Review Fluids*, vol. 6, p. 094603, Sep 2021.

43. M. H. Carpenter, J. Nordström, and D. Gottlieb, "A stable and conservative interface treatment of arbitrary spatial accuracy," *Journal of Computational Physics*, vol. 148, pp. 341–365, 1999.

44. W. J. Feiereisen, W. C. Reynolds, and J. H. Ferziger, *Numerical simulation of a compressible homogeneous, turbulent shear flow.* PhD thesis, Stanford Univ., CA., Stanford Univ., CA., Stanford Univ., CA., Mar. 1981.

45. S. Pirozzoli, "Numerical methods for high-speed flows," *Annual Review of Fluid Mechanics*, vol. 43, no. 1, pp. 163–194, 2011.

46. J. Williamson, "Low-storage Runge-Kutta schemes," *Journal of Computational Physics*, vol. 35, no. 1, pp. 48–56, 1980.

47. M. H. Carpenter and C. A. Kennedy, "Fourth-order 2N-storage Runge-Kutta schemes," *NASA Langley Research Center*, Jun 1994.

48. S. P. Jammy, C. T. Jacobs, and N. D. Sandham, "Performance evaluation of explicit finite difference algorithms with varying amounts of computational and memory intensity," *Journal of Computational Science*, vol. 36, p. 100565, 2019.

49. G. N. Coleman, J. Kim, and R. D. Moser, "A numerical study of turbulent supersonic isothermal-wall channel flow," *Journal of Fluid Mechanics*, vol. 305, pp. 159–183, 1995.

50. P. Bradshaw, "Compressible turbulent shear layers," *Annual Review of Fluid Mechanics*, vol. 9, pp. 33–54, 1977.

51. D. J. Lusher and N. D. Sandham, "Assessment of low-dissipative shock-capturing schemes for the compressible Taylor-Green vortex," *AIAA Journal*, vol. 59, no. 2, pp. 533–545, 2021.

52. E. Johnsen, J. Larsson, A. V. Bhagatwala, W. H. Cabot, P. Moin, B. J. Olson, P. S. Rawat, S. K. Shankar, B. Sjögreen, H. C. Yee, X. Zhong, and S. K. Lele, "Assessment of high-resolution methods for numerical simulations of compressible turbulence with shock waves," *Journal of Computational Physics*, vol. 229, no. 4, pp. 1213–1237, 2010.

53. A. J. Reynolds, "The prediction of turbulent Prandtl and Schmidt numbers," *International Journal of Heat and Mass Transfer*, vol. 18, pp. 1055–1069, 1975.

REPORT DOCUMENTATION PAGE	Form Approved OMB No. 0704–0188

1. REPORT DATE *(DD-MM-YYYY)*	2. REPORT TYPE	3. DATES COVERED *(From - To)*
01-07-2022	Technical Memorandum	

4. TITLE AND SUBTITLE
Numerical study of the turbulent Prandtl number in supersonic plane-channel flow – the effect of thermal boundary conditions

5a. CONTRACT NUMBER

5b. GRANT NUMBER

5c. PROGRAM ELEMENT NUMBER

6. AUTHOR(S)
David J. Lusher, Gary N. Coleman

5d. PROJECT NUMBER

5e. TASK NUMBER

5f. WORK UNIT NUMBER
109492.02.07.05.01

7. PERFORMING ORGANIZATION NAME(S) AND ADDRESS(ES)
NASA Langley Research Center
Hampton, Virginia 23681-2199

8. PERFORMING ORGANIZATION REPORT NUMBER

9. SPONSORING/MONITORING AGENCY NAME(S) AND ADDRESS(ES)
National Aeronautics and Space Administration
Washington, DC 20546-0001

10. SPONSOR/MONITOR'S ACRONYM(S)
NASA

11. SPONSOR/MONITOR'S REPORT NUMBER(S)
NASA/TM–20220010483

12. DISTRIBUTION/AVAILABILITY STATEMENT
Unclassified-Unlimited
Subject Category
Availability: NASA STI Program (757) 864-9658

13. SUPPLEMENTARY NOTES
An electronic version can be found at http://ntrs.nasa.gov.

14. ABSTRACT
Direct numerical simulation is used to investigate the turbulent Prandtl number Pr_t above cold (isothermal) and hot (adiabatic) walls in a family of supersonic channel flows. A range of Reynolds numbers and mean temperature/density variations is considered. The value of Pr_t away from the wall approaches 0.85 above both the isothermal and adiabatic walls, with the width of the $\mathrm{Pr}_t = 0.85$ region increasing with wall-variable-based Reynolds number Re_{τ_w} (the latter strongly affected by the thermal boundary condition). The variable, near-wall Pr_t profiles from both the present and previous, passive-scalar simulations collapse as a function of the semilocal y^* wall scaling proposed by Huang et al. [1], with the y^*-dependence weakly parameterized by Re_{τ_w}.

15. SUBJECT TERMS
Direct numerical simulation, supersonic wall-bounded turbulence, heat transfer, turbulent Prandtl number

16. SECURITY CLASSIFICATION OF:			17. LIMITATION OF ABSTRACT	18. NUMBER OF PAGES	19a. NAME OF RESPONSIBLE PERSON
a. REPORT	b. ABSTRACT	c. THIS PAGE			STI Information Desk (help@sti.nasa.gov)
U	U	U	UU	30	19b. TELEPHONE NUMBER *(Include area code)* (757) 864-9658